International Journal of Solids and Structures 256 (2022) 111948

Contents lists available at ScienceDirect

International Journal of Solids and Structures

journal homepage: www.elsevier.com/locate/ijsolstr

Experimental investigation of buckling stability of superelastic Ni-Ti tubes under cyclic compressive loading: Towards defining functionally stable tubes for elastocaloric cooling

Luka Porenta *, Jonas Trojer, Miha Brojan *, Jaka Tušek *

University of Ljubljana, Faculty of Mechanical Engineering, Aškerčeva 6, SI-1000 Ljubljana, Slovenia

ARTICLE INFO

Keywords:
Shape-memory
Elastocaloric effect
Buckling
Mode shape
Cyclic
Compression

ABSTRACT

Elastocaloric cooling technology recently attracted significant attention as an environmental friendly alternative to vapor-compression technology. It is based on the elastocaloric effect, which occurs in superelastic shape memory alloys (SMAs) during stress-induced martensitic transformation. To date, several proof-of-concept devices (mostly based on tensile loading) have been developed, but limited fatigue life was shown to be one of the major issues. Compressive loading improves the fatigue life of such devices significantly, but in return buckling of SMA structure might occur. To overcome this challenge, it is crucial to understand the buckling phenomena of SMA structures, especially for thin-walled tubes that seem to be ideal candidates for application in elastocaloric cooling devices. Here, we experimentally investigated the effects of the diameter-to-thickness ratio (D_{out}/t) and slenderness (λ) on buckling stability of Ni-Ti tubes that were subjected to cyclic compressive loading. In total, 161 superelastic Ni-Ti tubes with outer diameter (D_{out}) ranging from 2 mm to 3 mm, D_{out}/t ranging from 5 to 25 and gauge lengths (L_g) ranging from 6 to 20 mm were tested. The loading procedure consisted of 3 parts: (I) 1 isothermal full-transformation loading cycle, (II) 50 training cycles, and (III) 20 adiabatic cycles to simulate loading conditions in elastocaloric device. We constructed experimental phase diagrams of buckling modes in λ - D_{out}/t space for constant D_{out} and in λ - D_{out} space for constant D_{out}/t ratio. Marked areas of functionally stable tubes in these phase diagrams give the design guidance for future developments of durable and efficient elastocaloric devices and other applications, e.g. actuators and dampers.

1. Introduction

Shape memory alloys (SMAs) belong to a group of smart materials whose material properties change when acted upon by external stimuli. Among them Ni-Ti alloys are the most widely studied and applied (Jani et al., 2014). They exhibit two unique properties (Lagoudas, 2008): shape memory effect (SME) and superelasticity (SE). SME is the ability of the material to restore its original shape after being deformed and subsequently subjected to a temperature above austenitic transformation finish temperature A_f, while SE is the ability of the material at a temperature higher than A_f to withstand large (reversible) strains when subjected to an external stress. Both properties are attributed to the first-order solid-to-solid martensitic transformation from multi-variant, low-order, low-temperature product phase called martensite (M), to single-variant, high-order, high-temperature parent phase called austenite (A) and vice-versa. The transformation in the material can be induced by changing the temperature and/or stress. A typical (stress-induced) SE response upon loading includes an elastic response of A phase, transformation plateau, and an elastic response of M phase, while upon unloading a reverse transformation occurs, with a hysteresis behavior between forward and reverse transformation. These unique properties of SMA are utilized in several products and applications, such as actuators (Coral et al., 2012), dampers (Ozbulut et al., 2011), cardiovascular stents and orthodontic wires (Petrini and Migliavacca, 2011). Nevertheless, in recent years, another important SMA property — the elastocaloric effect (eCE), which is closely related to the SE, attracted significant interest. During the stress-induced martensite phase transformation (from A to M) at a temperature above A_f, the latent heat is released from the material to the surroundings, while during the reverse transformation heat flow is reversed. If loading/unloading occurs at a fast rate, released/absorbed heat can heat up/cool down the material, which is known as the elastocaloric effect. Recently, eCE attracted attention as an environmentally friendly alternative to vapor-compression technology (that is relatively inefficient and uses environmentally harmful refrigerants) (Moya et al., 2014; Kabirifar

* Corresponding authors.
E-mail addresses: luka.porenta@fs.uni-lj.si (L. Porenta), miha.brojan@fs.uni-lj.si (M. Brojan), jaka.tusek@fs.uni-lj.si (J. Tušek).

https://doi.org/10.1016/j.ijsolstr.2022.111948
Received 14 April 2022; Received in revised form 19 August 2022; Accepted 25 August 2022
Available online 31 August 2022
0020-7683/© 2022 The Authors. Published by Elsevier Ltd. This is an open access article under the CC BY-NC-ND license (http://creativecommons.org/licenses/by-nc-nd/4.0/).

et al., 2019) and was even recognized as the most promising future non-vapor-compression refrigeration technology by the US Department of Energy (Navigant Consulting Inc., 2014). In the last couple of years about 15 proof-of-concept elastocaloric devices have been built and tested and the best of them already demonstrated commercially relevant cooling characteristics (Schmidt et al., 2015; Tušek et al., 2016; Snodgrass and Erickson, 2019; Ulpiani et al., 2020; Greibich et al., 2021; Qian et al., 2016b; Bachmann et al., 2021; Ianniciello et al., 2022). The majority of elastocaloric devices are based on binary NiTi, however, in the last decade new elastocaloric materials are being developed rapidly. These materials can generally be divided into different groups, i.e. Ni-Ti-based SMAs (Tušek et al., 2015; Kim et al., 2018), Cu-based SMAs (Xu et al., 2016), Fe-based SMAs (Xiao et al., 2022), magnetic SMAs (Cong et al., 2019; Shen et al., 2020) and shape memory polymers (Xie et al., 2017; Coativy et al., 2020; Zhang et al., 2022). A comprehensive review of the elastocaloric materials can be found in (Kabirifar et al., 2019) and (Mañosa and Planes, 2017).

A typical elastocaloric cooling cycle is based on four basic operational steps, namely, adiabatic loading of the SMA material, heat transfer to the heat sink, adiabatic unloading of the SMA material, and heat transfer from the heat source (Qian et al., 2016a; Kabirifar et al., 2019; Chen et al., 2021). Most of the elastocaloric devices developed to date are based on tensile loading of SMA elements (Schmidt et al., 2015; Tušek et al., 2016; Kirsch et al., 2018). As shown in several studies (Engelbrecht et al., 2016; Tušek et al., 2018; Hou et al., 2018), tension stress promotes crack propagation during cyclic loading, which leads to fracture and failure already after a relatively low number of cycles. Limited fatigue life is currently one of the main bottlenecks of elastocaloric technology. On the other hand, SMA elements loaded in compression have significantly better fatigue life compared to tensile loading and do not exhibit fatigue fracture events after millions of loading cycles (Porenta et al., 2020b; Chen et al., 2019; Zhang et al., 2019). However, efficient and powerful elastocaloric devices require rapid and efficient heat transfer between SMA elements and heat transfer medium, which indicates that SMA structures must be thin-walled with a large heat transfer area. On the other hand, thin structures are prone to buckling, i.e. loss of stability and collapse. Therefore, a compromise between good heat transfer properties and functionally stable structural response has to be found and thin-walled tubes seem to be ideal candidates for that (Porenta et al., 2020b) and (Ahčin et al., 2021). In order to determine the optimal geometry of thin-walled SMA tubes for elastocaloric devices, buckling response of SMA tubes as well as other influencing factors, such as material parameters, geometry, supports, initial imperfections, etc., have to be studied in detail and well understood.

The main motivation for research of buckling stability of SMA elements in the past was their potential application as high-energy absorption dampers that could be used multiple times due to strain recovery. To our knowledge, the first investigation was performed by (Urushiyama et al., 2001), who axially loaded initially curved fully martensite Ni-Ti-Cu rods. They found that the rods first straightened at increasing load and afterwards buckled (failed as a rod). This phenomenon was named anti-buckling and was later also studied numerically in (Urushiyama et al., 2003) and (Richter et al., 2011). In later years, the majority of studies on buckling stability of SMA structures was focused on plates (Suzuki et al., 2004), rods (Rahman et al., 2001, 2005; Pereiro-Barceló and Bonet, 2017; Asfaw et al., 2020; Watkins et al., 2018) and particularly on tubes with circular cross-section (Nemat-Nasser et al., 2006; Tang and Li, 2012b,a; Watkins, 2015; Watkins et al., 2018; Damanpack et al., 2018; Jiang et al., 2016a,b; Porenta et al., 2020b; Xiao and Jiang, 2022), which are also the subject of our study. Among these, (Nemat-Nasser et al., 2006) conducted an experimental analysis, in which Ni-Ti thin-walled tubes (with outer diameter of the tube $D_{out} = 4.5$ mm and diameter-to-thickness ratio $D_{out}/t = 36$) of different lengths were quasi-statically and dynamically loaded in compression. During fast dynamic loading, a transition from local axially symmetric to asymmetric buckling mode shape was observed, while the tubes at quasi-static loading showed only local asymmetric buckling with 3 circumferential waves. (Tang and Li, 2012b) investigated buckling of superelastic Ni-Ti tubes ($D_{out} = 6.3$ mm and $D_{out}/t = 42$) of different lengths and different constraint conditions at both ends of the tube under quasi-static loading in compression. Similar to (Nemat-Nasser et al., 2006), local buckling with 3 circumferential waves was observed in the majority of cases. In the same study (Tang and Li, 2012b) numerical simulations of buckling using 3D solid finite elements (FE) were performed as well. A phase diagram of buckling mode shapes in L/D_{out} - D_{out}/t space (where L is length of the tube) was obtained by varying the geometry of the tubes. In further experiments, (Tang and Li, 2012a) investigated buckling of tubes of different lengths with 3 different cross-sections, i.e. $D_{out} = 6.3$ mm and $D_{out}/t = 42$, $D_{out} = 6$ mm and $D_{out}/t = 30$, $D_{out} = 5.3$ mm and $D_{out}/t = 25.4$, which were subjected to dynamic loading. Buckling mode transition, similar as in (Nemat-Nasser et al., 2006), was observed during loading. (Watkins, 2015) and (Watkins et al., 2018) isothermally compressed superelastic Ni-Ti tubes ($D_{out} = 3.176$ mm and $D_{out}/t = 10$) of different lengths and compared the responses to superelastic SMA rods with similar slenderness (λ). They concluded that longer tubes tend to buckle approximately at the beginning of the transformation and that further loading results in ovalization of the cross-section, followed by kinking and snap-through buckling. Shorter tubes, on the other hand, exhibited buckling–unbuckling phenomenon (BUB), where the structure first starts to buckle globally during loading and then starts to straighten back even though the axial load is further increasing. A more detailed investigation of BUB can be found in (Watkins and Shaw, 2018) and (Xiao and Jiang, 2022). (Damanpack et al., 2018) numerically investigated the influence of geometric imperfections and tube length on buckling stability. They used experimental results from (Watkins, 2015) as a reference. Simulations were performed using 3D solid FE and finite strain material model in order to efficiently capture also the post-buckling response. In (Jiang et al., 2016a,b) experimental and numerical investigation of stability of a Ni-Ti tube ($D_{out} = 6.32$ mm and $D_{out}/t = 23.6$) with length of 19.6 mm was carried out. In the numerical part, sensitivity analysis for initial geometric imperfection was done first, followed by simulation of the experiment. The results showed good agreement with the experimental results, where local buckling with 3 circumferential waves was observed. Nevertheless, the only investigation for the purpose of elastocaloric technology focused on buckling was performed in (Porenta et al., 2020b), where Ni-Ti tubes ($D_{out} = 3$ mm and $D_{out}/t = 12$) of different lengths were cyclically loaded in compression. To assure uniaxial loading and fixed supports at the ends of the tube, the authors used a special clamping device. They showed that mid-length tubes buckled only after first enduring a few loading cycles with stable response. Moreover, numerical predictions of critical buckling stress for different end constraint conditions of the tube and different lengths were made by developing a simple 1D numerical model.

So far, there has rarely been any systematic investigations of the stability of tubes with different D_{out}/t ratios at constant D_{out} or with different D_{out} at constant D_{out}/t ratio. As reported in (Porenta et al., 2020b) tube instability can arise after a few loading cycles. Therefore, it is crucial to investigate the response of the tube for multiple cycles. Thus, the goal of this study is to construct experimental phase diagrams of buckling mode shapes and areas of functionally stable tubes in λ - D_{out}/t space for constant D_{out} and in λ - D_{out} space for constant D_{out}/t ratio for tubes subjected to cyclic compressive loading. We define a functionally stable tube as a tube that serves its purpose, in our case the ability of cyclic generation of eCE by reaching the end of transformation, while still enduring some degree of instabilities. The second goal of this study is to obtain isothermal stress–strain curves of the first loading cycles that can be used in the future as a reference in numerical simulations for predicting buckling of thin-walled SMA tubes.

Table 1
Labels, dimensions, transformation temperatures, and number of the tubes used in the experiments.

Label	D_{out} (mm)	D_{in} (mm)	D_{out}/t	L_g(mm) | step size	A_f (°C)	Number of tested tubes
D3	3.0 ± 0.007	2.5 ± 0.015	12	10–20 | 2 mm	−4.0 ± 0.1	26
Dt25	2.5 ± 0.009	2.3 ± 0.017	25	6–14 | 4 mm	−6.3 ± 0.8	22
Dt17	2.5 ± 0.008	2.2 ± 0.013	16.67	6–14 | 2 mm	−5.5 ± 0.1	22
Dt12	2.5 ± 0.004	2.08 ± 0.008	11.9	10–16 | 2 mm	−9.8 ± 0.1	15
Dt10	2.5 ± 0.002	2 ± 0.021	10	10–18 | 2 mm	−7.5 ± 1.3	24
Dt5	2.5 ± 0.002	1.5 ± 0.012	5	10–18 | 2 mm	−4.8 ± 0.3	28
D2	2.0 ± 0.006	1.67 ± 0.019	12.12	6–14 | 2 mm	−7.0 ± 2.8	24

The rest of the paper is organized in the following way: In Section 2, the sample preparation and the experimental procedure are described. In Section 3, the results of the experiments are presented and discussed, while the conclusions are drawn in Section 4.

2. Experiments

2.1. Samples and sample preparation

Medical grade Ni-Ti tubes of 55.96 wt% Ni (55.92 wt% Ni for D3 tube), with length of 100 mm, D_{out} ranging from 2 mm to 3 mm and D_{out}/t ranging from 5 to 25, were supplied by Memry corporation (SAES Group). Our selection of tubes' dimensions was based on the recent elastocaloric prototypes, in which similar tubes were used (see e.g. (Porenta et al., 2020b; Ahčin et al., 2021; Bachmann et al., 2021; Ianniciello et al., 2022) and (Qian et al., 2016b)). In Table 1, dimensions and transformation temperatures of all the tubes used in our experiments are gathered. The transformation temperatures A_f were measured by the supplier according to ASTM F2082 using a bend-free recovery test. Fatigue life and eCE of D3 tube were evaluated in (Porenta et al., 2020b). The tubes can be divided into two groups. The first group includes the tubes with constant D_{out} = 2.5 mm and D_{out}/t ranging between 5 and 25. These tubes are labeled as Dt*XX*, where *XX* stands for approximate value of D_{out}/t ratio. The tubes in the second group have D_{out}/t ratio of approximately 12 and D_{out} of 3, 2.5 and 2 mm and are labeled D3, Dt12, and D2, respectively. Note that label Dt12 could be replaced by label D2.5, however, to have unique labels, only the Dt12 label is used throughout the paper. In total, we tested 161 samples with gauge lengths (L_g) ranging from 6 to 20 mm using 2 mm steps (and 4 mm steps for Dt25 tube). In Table 1 step size refers to the steps of gauge lengths of tested tubes, e.g. step size of 2 mm for D3 tube means that we tested tubes with gauge lengths of 10, 12, 14, 16, 18, and 20 mm. The supplied tubes were cut to the desired length using Buehler IsoMet low-speed diamond saw at low cutting force in order to avoid overheating of the material that can cause microstructural changes and loss of superelasticity. The cut surface of the tube was further polished to the exact length ±0.04 mm with Buehler EcoMet30 using grit P800. Polishing also deburred the edges of the tube (see Fig. 1) and more importantly, it ensured that the end faces of the tube are perpendicular to its axis. The last step of sample preparation was painting the gauge surface first with a white color and then spraying over a pattern of black speckles in order to use an in-house developed video-extensometer (VE) to measure displacements on the tube and calculate the strains in post-processing (details about accuracy and derivation of uncertainties of the VE strain measurements are given in Appendix A). For tubes Dt5, Dt12, and Dt25 analysis of microstructure was performed in order to assess the grain size. Results are presented in Appendix B.

2.2. Experimental setup

Experiments were performed on a Zwick Z050 universal testing machine (UTM), equipped with an Xforce P load cell with measuring range ±5 kN and accuracy of ± 0.5% of full scale, while positioning of the cross-head is accurate to ± 1 μm. A special clamping mechanism, as shown schematically in Fig. 2 (inset), was designed to provide collinear and fixed supports at both ends of the tube as well as to assure uniaxial movement of the upper edge of the tube in the direction of the tube's axis. Fixed support was provided by the ER11 collet that grips and holds the tube on the outside surface, thus preventing rotation and a non-axial movement. To prevent buckling and ovalization of the tube during tightening of the nut of the ER collet, a pin of length L_{collet} = 10.5 mm (14.6 mm for D3 tubes) was placed inside the tube at both ends with the tight fit to avoid its movement in the axial direction (see the inset in Fig. 2). The length of the pins matches the length of the tube's part that is inside the collet. The nut of the ER collet was tightened with a torque at 14 Nm, set according to recommendations of the manufacturer of the ER collets (RegoFIX).

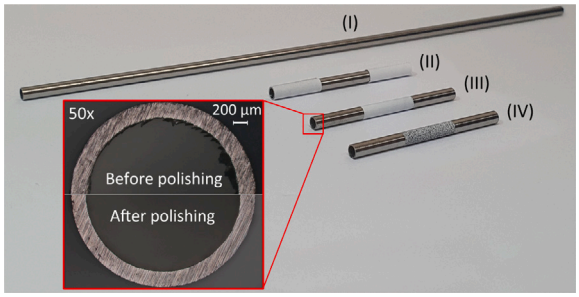

Fig. 1. Process of sample preparation: (I) a full-length tube, as received, (II) cut tube with polished edges and protection tapes ready for painting, (III) white painted tube, and (IV) pattern painted tube. Inset shows the cut end face before and after the polishing at 50× magnification.

Due to the small size of the sample and the lack of space for the use of a contact extensometer on the sample we used a VE developed in-house to measure displacements and determine the strains of the tubes. Our VE device comprises a 6K Panasonic LUMIX DC-GH5L camera with Olympus M.Zuiko digital ED (60 mm, f/2.8) macro lens and software for processing the images developed in Python (mainly by using the OpenCV library). The whole experimental setup is shown in Fig. 2. It is important to mention that lightning for the VE is crucial for obtaining good results. Therefore, primary diffusive and secondary direct lighting were used. The position of the former is at the same level as the clamped tube in the UTM, while the position of the latter is above and below the tube level to illuminate the surface of the tube near the supports. The average uncertainties of the strain measurements were 0.041% (see Appendix A for details).

2.3. Experimental procedure

The goal of the experiments was to determine the tube lengths for different cross-sections that endure full transformation without a failure, before using them in elastocaloric regenerator, such as (Ahčin et al., 2021), where SMA elements are cyclically loaded. In this work, a failure of the tube is considered to be the loss of the ability to serve its function, which means inability of the tube to reach the end of transformation (1150 MPa) due to buckling. As mentioned before, failure of the tube can occur after a few (training) loading cycles, even though the response of the tube seems to be stable in the first loading cycle (Porenta et al., 2020b). Therefore, our experiments consisted of

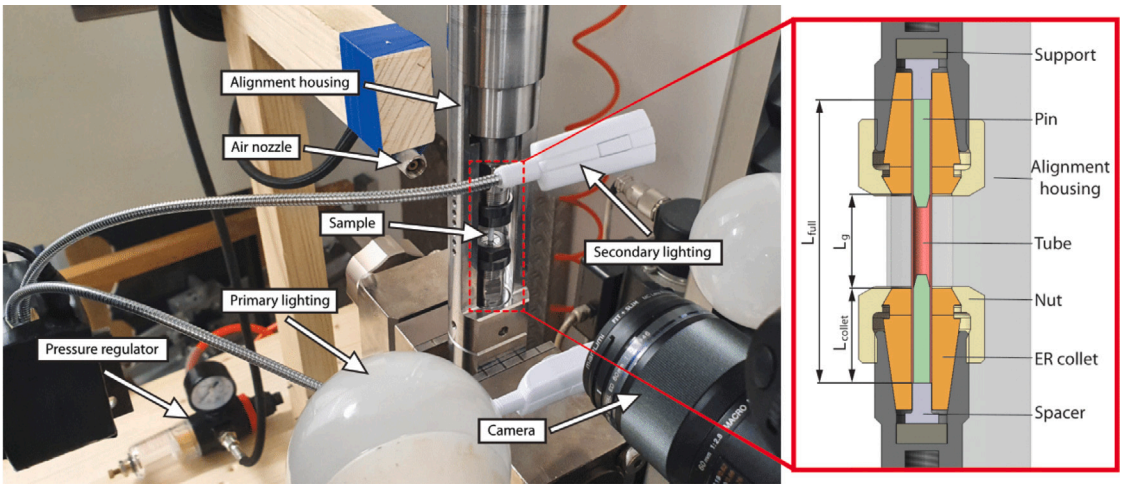

Fig. 2. The experimental setup comprises a photo camera, primary and secondary lighting, and a system for forced convection with a pressure regulator and the air nozzle. Inset: cross-section of a sample clamping mechanism with labeled important constituent elements and marked lengths.

three loading parts: 1 isothermal cycle, 50 training cycles, and 20 adiabatic cycles. Before each loading part, a preload was applied to ensure that all parts of the clamping device fit well and all air gaps are removed. During the preload, the tube was loaded from 0 to 230 MPa and unloaded back to 10 MPa at a strain rate of 0.001 s^{-1} with 10 s holding time in the unloaded position. The latter is necessary for synchronization between the UTM and VE measurements.

In the isothermal cycle the tubes were loaded from 10 to 1150 MPa (corresponding to the end of the transformation) and unloaded back to 10 MPa at a strain rate of 0.0003 s^{-1} (loading speed can be calculated based on L_g, see inset in Fig. 2), which was selected based on preliminary tests explained in Appendix C. The conditions (strain rate) are assumed to be isothermal when the temperature changes are below 1 °C. Note that in case of failure the stress of 1150 MPa was not reached and loading sequence was manually interrupted by enforcing the unloading sequence. The goal of the isothermal test was to obtain isothermal stress–strain curves that will serve as a reference in future numerical simulations, see e.g. (Porenta et al., 2020a, 2021). During the isothermal tests, the strains of the tube were measured by the VE with the sample rate of 1 Hz. For the tubes that exhibited no failure, the test continued with 50 training cycles in order to obtain the stable stress–strain response of the tube. At this stage, the tubes were loaded from 0 to 1150 MPa at a strain rate of 0.008 s^{-1}. Note that the training strain rate was chosen such that it is slow enough and does not generate large temperature changes due to the elastocaloric effect during loading and unloading. Since the tube was subjected to forced convective heat transfer during the training, the selected strain-rate was allowed to be higher than in our previous studies, where forced convection was not applied (Porenta et al., 2020b). Significantly lower strain-rate would prolong the entire experimental procedure drastically. During this part, we collected the information about the buckling mode shape and the cycle number at which failure occurred.

For the surviving tubes, the third part (adiabatic cycles) commenced. To avoid the problem of overshooting with the UTM force control feedback loop at high displacement rates the displacement control was used in adiabatic tests. The tubes were loaded between 0.1 mm and the maximum relative displacement of the last training cycle at a strain rate of 0.07 s^{-1} (that fulfilled adiabatic conditions as shown in Supplementary information of (Porenta et al., 2020b)). According to the preliminary tests (see Appendix C) a holding time of 10 s at constant displacement was applied after each load level change in order to stabilize the sample's temperature with the surroundings before changing the load level again. The goal of the adiabatic tests was to simulate the loading conditions that normally occur in elastocaloric devices, where the SMA elements are loaded at high strain rates (usually close to adiabatic conditions).

It is important to mention that during all three loading parts the tubes were exposed to forced convection with air that assured isothermal conditions during the first loading part, smaller temperature changes during training, and faster temperature stabilization during the holding time of adiabatic cycles (see Appendix C for more details).

3. Results & discussion

3.1. Stress–strain diagrams

As mentioned in Section 2.3, strains of the tube were measured by the VE during the isothermal loading cycle. More specifically, two regions of interest (ROIs) were defined on the tube during the VE data analysis (see Fig. A.14). One near the top edge (ROI1) and the other near the bottom edge (ROI2). Initial distance in the first captured frame (in pixels) between centers of ROIs is L, while relative displacements of them in the following frames are: $\Delta L = p_{ROI2} - p_{ROI1}$, where p_{ROI1} and p_{ROI2} are the relative centers' positions of ROI1 and ROI2, respectively. Axial strain is further defined as: $\varepsilon = \Delta L/L$. The reader is referred to Appendix A for details on strain determination and evaluation of its uncertainty. It must be emphasized that the source of error due to out-of-plane buckling near the supports is not included in our evaluation of uncertainty of VE strain measurements, therefore, all post-buckling VE strains have an unknown degree of error. With synchronization of UTM force measurements and VE strain measurements stress–strain curves can be obtained, as shown in Fig. 3. We used engineering stress: $\sigma = F/A$, where F is the axial force measured by UTM and A is the initial cross-section area of the tube. In Fig. 3 only representative stress–strain curves for each geometry of the tube are shown. Note that compressive stresses and contractions are taken as positive. These curves can be used as a reference in numerical simulations of buckling or for material parameters identification. Note that L_g indicates the distance between the supports (see the inset in Fig. 2), while L is the initial distance in pixels between the centers of ROIs.

From the stress–strain curves elastic modulus of austenite E_A can be assessed. In Table 2 average elastic moduli with standard deviations (represented by s) are gathered. The average value of all elastic moduli is approximately 70 GPa, which is in accordance with the literature (e.g. (Šittner et al., 2014)). Slight differences between the tubes can be attributed to the manufacturing process, where each tube is subjected to different stages of deformation (tubes are gradually drawn and annealed, however, the exact process is unknown). Tubes D3 and Dt17 have a slightly smaller elastic modulus than the rest. Nevertheless, the Dt25 tube stands out due to the large standard deviation of its elastic modulus. One reason for this may be the fact that at this D_{out}/t the

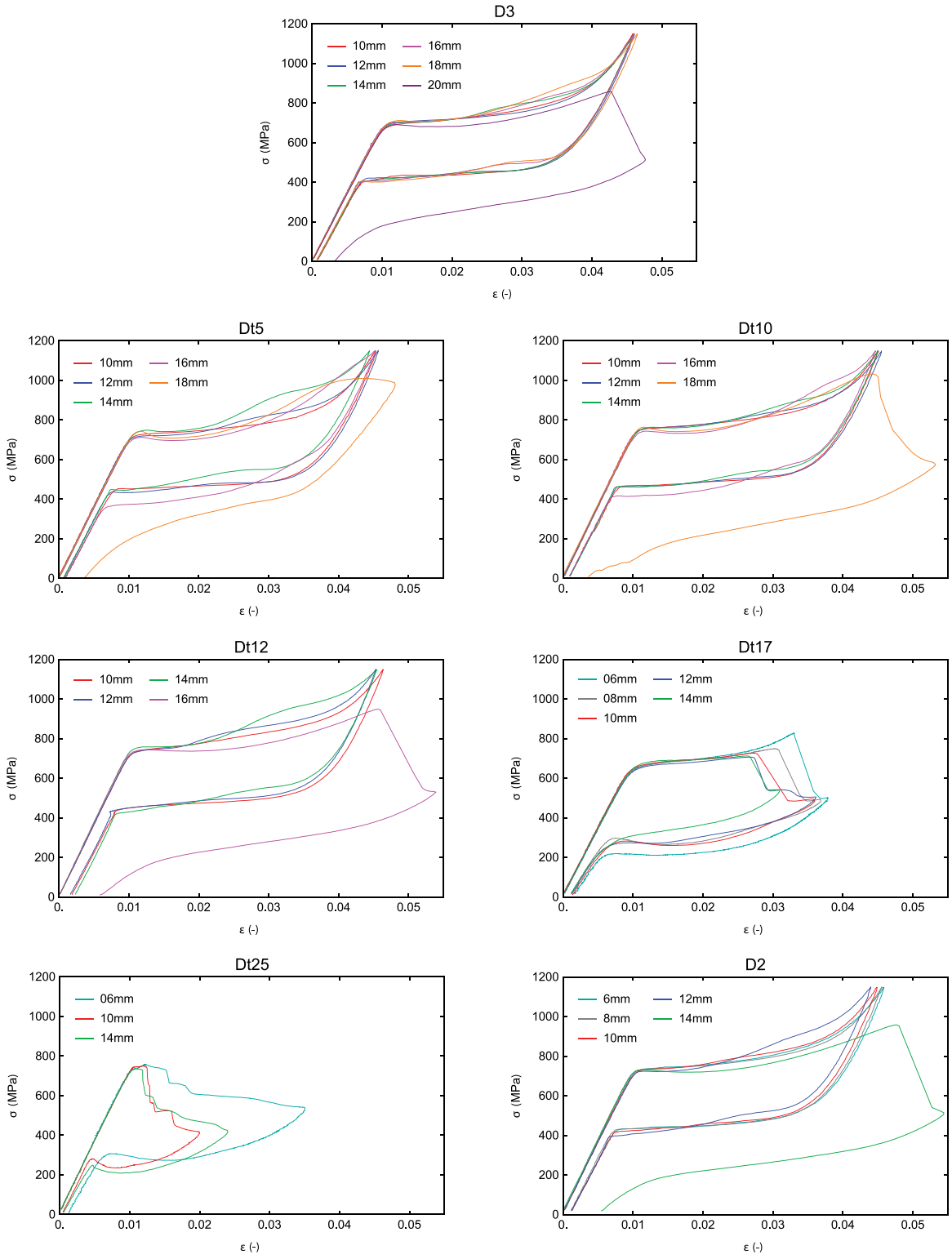

Fig. 3. Isothermal stress–strain curves of tubes with different cross-sections and gauge lengths, where D3 and D2 labels indicate outer diameter of the tube: 3 mm and 2 mm, respectively (at $D_{out}/t = 12$), and Dt labels indicate D_{out}/t ratio at $D_{out} = 2.5$ mm.

effects of geometric imperfections (over which we have no control) start to noticeably affect the response of the tube already at the beginning of loading, which in turn causes greater variation in the slope of the initial, i.e. elastic part of the stress–strain curve. Furthermore, for the shortest tubes of each cross-section the mean stresses at the beginning of transformation $\overline{\sigma}_{tr,s}$ were assessed from the stress–strain curves. The tangent intersection point method was applied for that purpose, where two tangents are fitted to the linear elastic and transformation part of the curve, with the stress at the beginning of transformation $\sigma_{tr,s}$ being the stress value at which the two tangents intersect. Note that responses

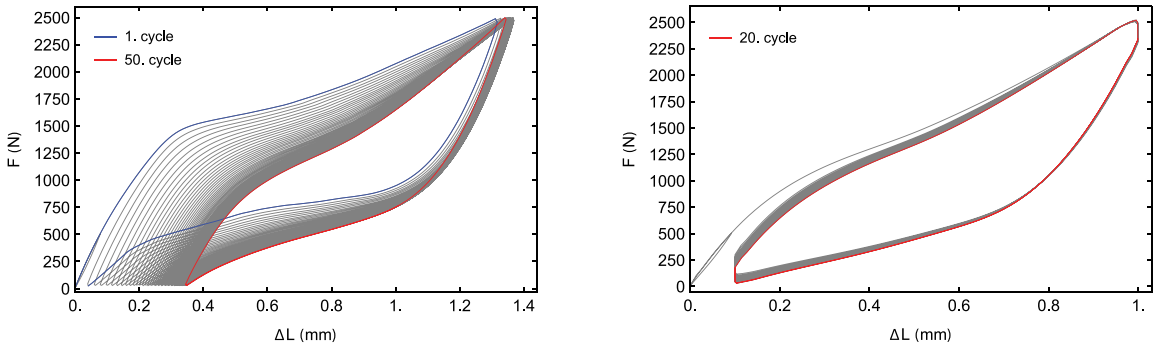

Fig. 4. Representative superelastic response of tubes during: training (left) and adiabatic cycles (right).

Table 2
Average elastic moduli and average stresses of the beginning of the transformation with both of their standard deviations.

Tube	$\overline{E}_A$ (MPa)	$s\left[E_A\right]$ (MPa)	$\overline{\sigma}_{\mathrm{tr,s}}$ (MPa)	$s\left[\sigma_{\mathrm{tr,s}}\right]$ (MPa)
D3	68 373	163	693	7.8
Dt25	71 864	3488	714	22.0
Dt17	68 036	291	670	10.5
Dt12	73 332	180	731	4.9
Dt10	71 875	407	748	10.5
Dt5	71 587	192	721	11.4
D2	72 076	325	724	9.5

of the shortest tubes were used for the determination of $\overline{\sigma}_{\mathrm{tr,s}}$ due to their least unstable response (compared to the longer tubes). In Table 2 mean stress values and their standard deviations are presented.

Fig. 4 shows a typical response of the tube during cyclic loading. Specifically, the presented responses were obtained by D3 tube with the gauge length $L_{\mathrm{g}} = 10$ mm. Since the strains during training and adiabatic loading were not measured by the VE, the responses are presented in force–displacement diagrams, where F is the axial force and ΔL are displacements of the crosshead, which also includes elastic deformations of UTM and clamping mechanism. In Fig. 4 (left), there is observable cyclic degradation of the superelastic response during training (Tušek et al., 2015; Miyazaki et al., 1986): (I) size of hysteresis is decreasing, (II) the beginning of the plateau during loading is less noticeable, while the stress at the beginning of the plateau is decreasing, (III) the overall slope of the response is rising and (IV) residual strains are decreasing towards 0. For this specific case the maximum relative displacement of the last training cycle is approximately 1 mm (between 0.35 mm and 1.35 mm) and the same limit was also set in the subsequent adiabatic loading as shown on Fig. 4 (right). During adiabatic loading there is additional stabilization of the superelastic response due to higher temperature changes, which were not present during training.

3.2. Phase diagrams

Response to compressive loading can be stable or unstable. During our experiments, we came across several different responses that can be divided into three groups: stable, globally unstable, and locally unstable.

Tubes with stable response survived all parts of the loading procedure without any observed instabilities on the VE recordings. However, based on (Watkins et al., 2018), where measurements using digital image correlation showed inhomogeneous strain distribution across the short tube loaded in compression, one must be aware that there might exist undetectable instabilities by our procedure. The stable response of the tube is shown in Fig. 5 and is labeled as SR. Note that in Fig. 5 there is a shadow visible in the middle of the tube due to the nut of the ER collet and should not be mistaken for buckling. Similarly, in the case

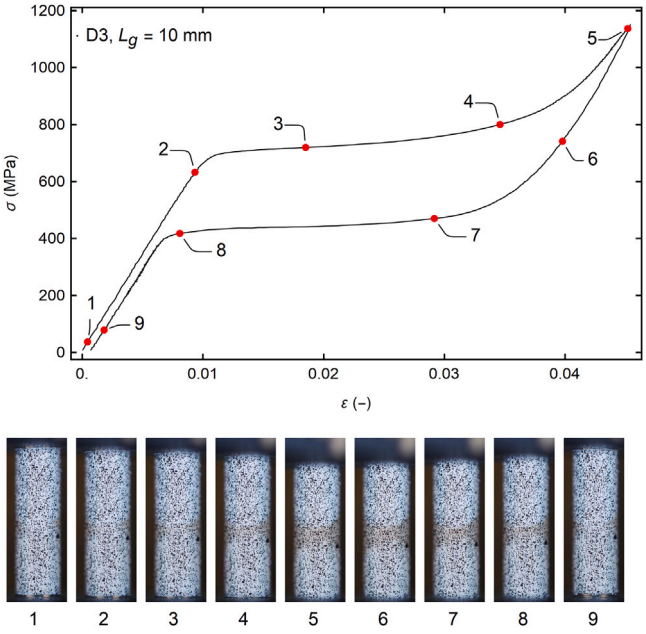

Fig. 5. Isothermal stress–strain diagram with characteristic points and corresponding camera-recorded deformations of the tube that exhibit stable response without buckling–unbuckling phenomena labeled as SR (the shadow visible in the middle of the tube is not due to buckling).

of longer tubes shadows are visible near the supports (see e.g. Fig. 6, however, VE measurements are not affected by the shadows.

Globally unstable tubes showed global (beam-like) buckling response at the beginning of the transformation, which in most cases results in a drop of the force followed by its increase. However, we noticed three different possible scenarios upon further loading. First, if the tube is stiff enough, unbuckling without failure occurs after the initial buckling, which characterizes a transitional buckling event, as shown in Fig. 6. Note that in this specific case the stress–strain curve is monotonically increasing during loading. This type of buckling mode is labeled as BUB (buckling–unbuckling). On the other hand, in the case of longer tubes after the initial buckling and force drop, the tubes may continue to buckle while the force is increasing, as shown in Fig. 7 and Fig. 8. During buckling, lateral displacements of the middle part of the tube are increasing and the cross-section of the tube starts to ovalize. At some point, the maximum force is reached, followed by the force decrease, indicating the failure. As shown in Fig. 7 for thinner tubes the force decrease is sudden and is attributed to the snap-through phenomenon that belongs to the group of local instabilities (the transition from global to local buckling occurs). This type of buckling is labeled as GB + LB1 (meaning global buckling followed by a local snap-through with 1 circumferential wave). On the contrary, thicker tubes

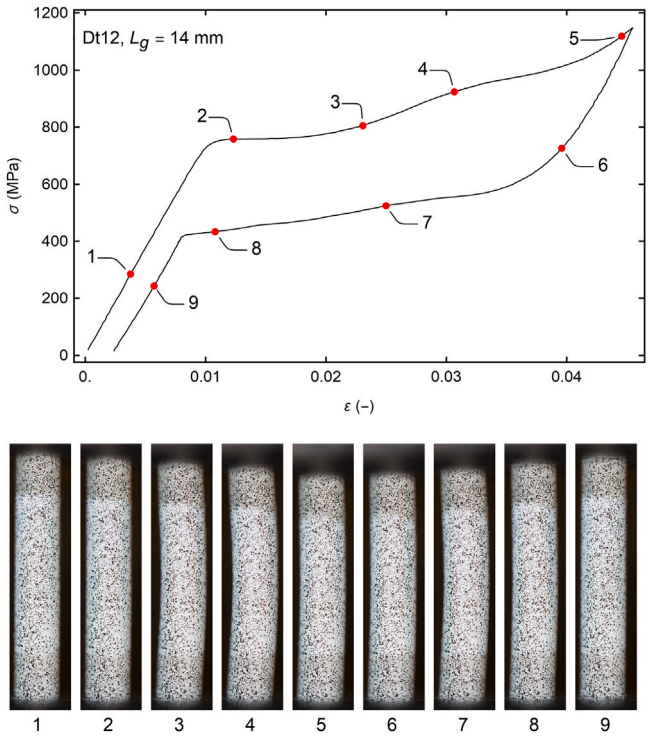

Fig. 6. Isothermal stress–strain diagram with characteristic points and corresponding camera-recorded deformations of the tube that exhibit global buckling with buckling–unbuckling phenomena labeled as BUB.

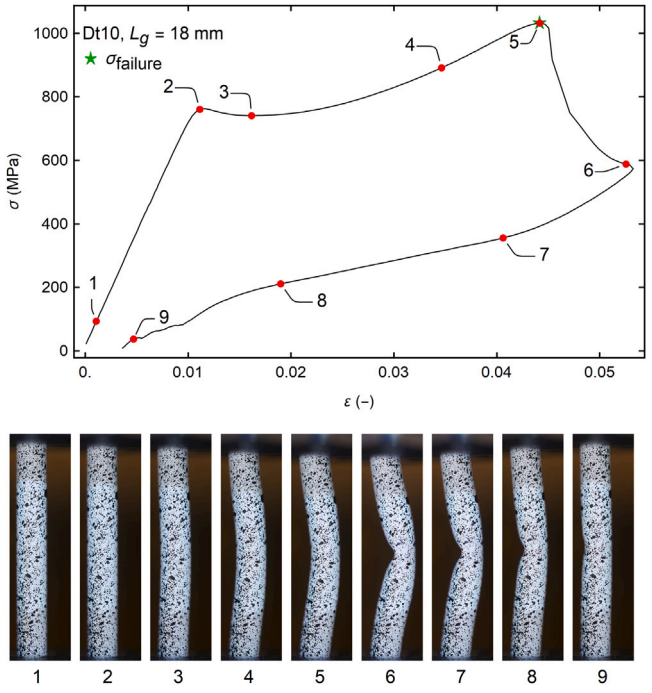

Fig. 7. Isothermal stress–strain diagram with characteristic points and corresponding camera-recorded deformations of the tube that exhibit combination of global and local buckling labeled as GB + LB1.

from our set exhibit a slow decrease of force and no snap-through, as shown in Fig. 8. This type of global buckling mode is labeled as GB. It is important to mention that it is expected that thicker tubes would also exhibit local snap-through phenomena, however, in our case the unloading started before it occurred.

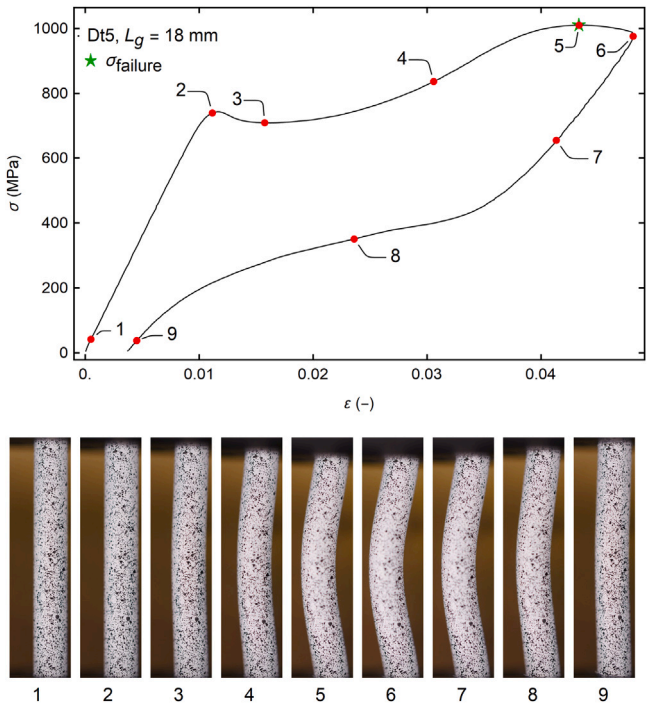

Fig. 8. Isothermal stress–strain diagram with characteristic points and corresponding camera-recorded deformations of the tube that exhibit global buckling only labeled as GB.

Locally unstable tubes showed many buckling mode shapes among which we were able to categorize two specific ones. Local buckling with 2 circumferential waves, as shown in Fig. 9, labeled as LB2 and mode shape with 3 circumferential waves as shown in Fig. 10, labeled as LB3. All other local buckling mode shapes are considered to be uncategorized and are labeled as LB. See Appendix D for further examples of different uncategorized local buckling modes. Interestingly,

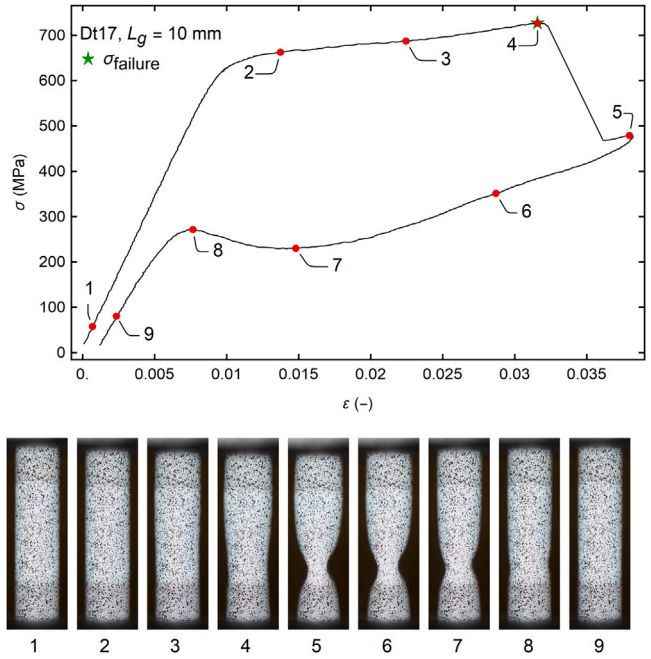

Fig. 9. Isothermal stress–strain diagram with characteristic points and corresponding camera-recorded deformations of the tube that exhibit local buckling with two circumferential waves labeled as LB2.

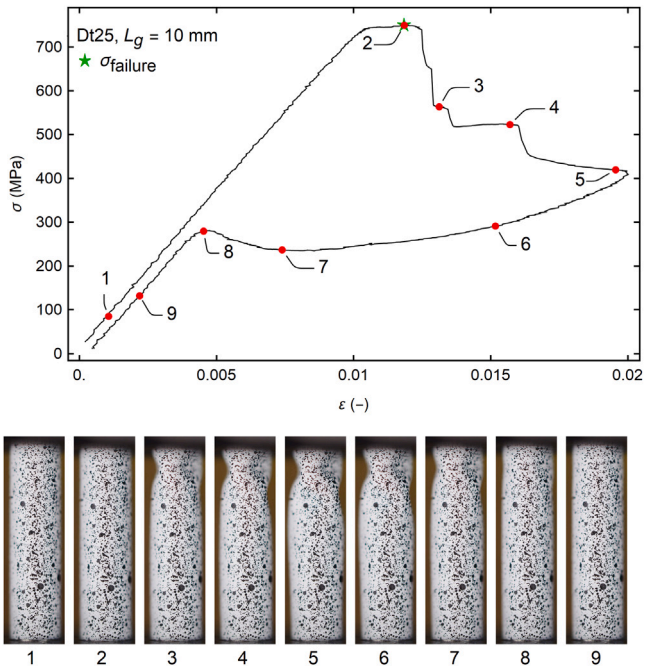

Fig. 10. Isothermal stress–strain diagram with characteristic points and corresponding camera-recorded deformations of the tube that exhibit local buckling with three circumferential waves labeled as LB3.

we observed that LB2 never appeared near the supports (but rather towards the middle of the tube), while LB3 is more likely to form near the supports. Note that online Supplementary data contains videos of all different buckling mode shapes observed in our isothermal tests.

In Fig. 11 (a) a phase diagram of buckling modes is shown for λ - D_{out}/t space at fixed D_{out} = 2.5 mm, while Fig. 11 (b) shows a phase diagram of buckling modes for λ - D_{out} space at approximately constant ratio $D_{out}/t = 12$. The slenderness λ is defined as

$$\lambda = \frac{L_g}{\sqrt{I/A}}, \quad \text{where} \quad I = \frac{\pi}{64}\left(D_{out}^4 - D_{in}^4\right) \quad \text{and}$$
$$A = \pi\left(\frac{D_{out}^2}{4} - \frac{D_{in}^2}{4}\right), \tag{1}$$

while I is the second moment of the cross-section and A is its area. Both diagrams in Fig. 11 show buckling mode shapes at failure regardless of the part of the loading procedure and regardless of the number of loading cycles at which the failure occurred. The colors of the pie charts and numbers inside them refer to the buckling mode shapes and the corresponding number of samples experiencing it, respectively. Circular-shaped pie charts indicate the BUB phenomenon was not observed during the isothermal cycle, while a star-like shape implies that BUB occurred. From Fig. 11 it is possible to determine which tubes have failed during the isothermal cycle, i.e. tubes marked with non-green circular-shaped pie chart, while the exact number of cycles to failure for each geometry is presented in Section 3.3. Finally, approximate regions of functionally stable, locally, and globally unstable tubes can be determined graphically on the phase diagrams. As mentioned above, functionally stable tube is a tube that serves its purpose (in our case the ability of cyclic generation of eCE by reaching the end of transformation, i.e. 1150 MPa), while still enduring some degree of instabilities. Functionally stable tubes can therefore exhibit SR or BUB.

In Fig. 11 (a) GB and GB + LB1 buckling mode shapes are prevalent above the solid black line, while below the dashed black line the region, where BUB is prevalent at isothermal cycle, could be defined. Below the slenderness of $\lambda \approx 15$ and between $D_{out}/t = 12$ and $D_{out}/t = 17$ there is a transition region (colored in yellow) from area of functionally stable tubes to area of locally unstable tubes. Below the solid black line and on the left-hand side of the transition region, there is an area of functionally stable tubes. Note that maximal length of functionally stable tubes decreases from 14 mm to 12 mm by increasing the D_{out}/t ratio from 5 to 12. At the applied experimental conditions it turned out that the highest D_{out}/t that still yields functionally stable tubes is 12. At the right-hand side of the transition region and below the full black line, there is an area of locally unstable tubes. For Dt17 tubes, the LB2 mode shape is prevalent, while shorter Dt25 tubes (shorter than 10 mm) have a prevalent LB3 buckling mode shape. Longer Dt25 tubes (10 mm and longer) mostly exhibit uncategorized local buckling. The difference in mode shapes for these tubes is likely due to uncertainty of geometric imperfections already mentioned before as a possible reason for the relatively high elastic modulus standard deviation for this tube type. This can be seen only for Dt25 tubes since they are the most thin-walled and therefore the most susceptible to imperfections.

In Fig. 11 (b) the area of functionally stable tubes is located below the convex black curve, while above the concave black curve dominates the GB + LB1 mode shape. Between these lines, the combinations of stable, globally and locally unstable responses can be observed. For D3 tubes (and those with larger D_{out}) local buckling might be prevalent for mid-length tubes as indicated by the D3 tube with the gauge length of L_g = 14 mm. The most fascinating observation is that the longest functionally stable tubes with $D_{out}/t = 12$ have D_{out} = 2.5 mm, while the length of functionally stable tubes is decreasing with changing the outer diameter. It must be emphasized that there could exist a longer functionally stable tube with $D_{out}/t = 12$ in the vicinity of the outer diameter of 2.5 mm. Another interesting finding is that tubes with slenderness lower than approximately 11 do not show BUB.

3.3. Impact of cycling loading on the failure

As mentioned in literature (Porenta et al., 2020b) failure of the tube can occur after a few loading cycles and not necessarily only in the first cycle. Similar trend was experienced also during our experiments, where majority of unstable tubes failed during training. One of the reasons for the failure of the tube during cyclic loading could be the accumulating formation of the residual martensite in each cycle as shown in Fig. 4 (left). This could affect the stress and strain distribution through the tube, causing the progressive behavior of BUB, which means lateral displacements in each cycle are increasing, leading to failure. However, further investigations are required to fully understand this phenomenon.

In Fig. 12, the number of cycles to failure for each tube are shown as a function of gauge length. Labels on the left-hand side of the diagrams refer to the part of the loading procedure during which failure occurred, while numbers on the right-hand side represent the cycle number of the particular part of loading procedure. Call-out indications represent the number of identical tubes that failed at the same cycle number. In the diagrams, functionally stable tubes that showed no failure through the whole loading procedure are marked.

Wider span of lengths between functionally stable tubes and tubes that failed in the isothermal cycle is observed for D3 and D2 tubes. More specifically, D3 tubes are functionally stable at gauge length of 10 mm, while the majority of 20 mm long D3 tubes failed during isothermal loading. Similarly, all D2 tubes of gauge length 14 mm failed at isothermal loading cycle, while 6 mm long tubes are functionally stable. In the regions between these lengths failure might occur in some cases during training or adiabatic loading. On the other hand, the repeatability of failure of Dt5, Dt10 and Dt12 tubes is more reliable and the span of lengths between functionally stable tubes and tubes that failed in the isothermal cycle is narrower compared to D2 and D3 tubes. The reason for failure at different cycles of identical tubes is the randomness of imperfections. Therefore, in order to determine functionally stable tubes multiple identical tubes must be tested. It is worth to mention, that the Dt17 and Dt25 tubes failed at the first isothermal loading cycle, with one exception of the Dt17 tube of gauge

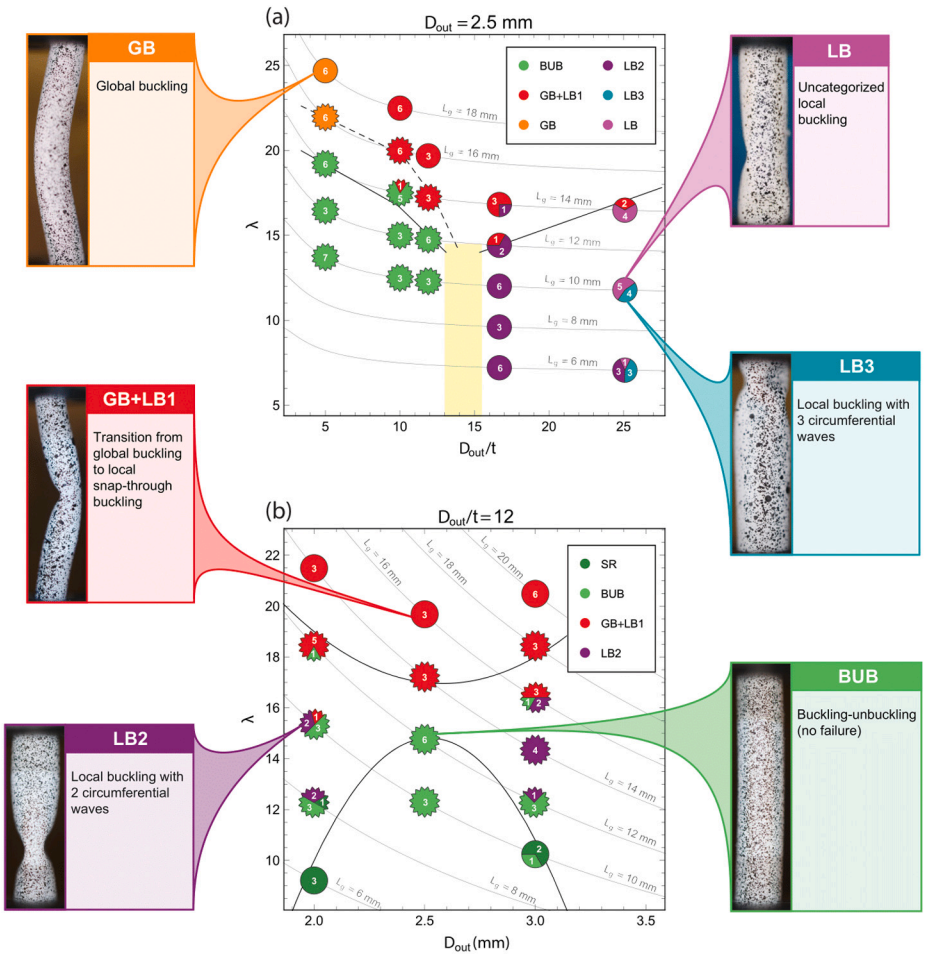

Fig. 11. Phase diagram of buckling mode shapes with images of representative buckling modes and marked characteristic areas: (a) for the tubes of constant $D_{out} = 2.5$ mm for λ - D_{out}/t space and (b) for the tubes of approximately constant ratio $D_{out}/t = 12$ for λ - D_{out} space. Star-like pie charts indicate BUB in the isothermal loading cycle and circle pie charts indicate that BUB was not observed.

length 6 mm that failed at the first training cycle. Interestingly, the majority of the tubes that survived training also survived adiabatic loading cycles. Therefore, training alone might be a suitable indicator for determining the functionally stable tubes.

3.4. Buckling stresses

For the isothermal response of the tube the axial stress of the first instability σ_{first} and the maximal stress $\sigma_{failure}$ for the tubes that failed can be determined with the help of synchronization of UTM and VE measurements. Specifically, the first instability, i.e. the first visible lateral displacement, is determined by the eye from the VE images and the corresponding stress σ_{first} is then recorded. Note that the tube has no preferred buckling direction and lateral displacement perpendicular to observation direction is easily visible, while displacements towards and away from the VE are visible as the central part of the tube is out of focus. On the other hand, the maximal stress $\sigma_{failure}$ is the stress that the tube can withstand before failure, i.e. monotonic stress decrease (see Figs. 7–10).

Fig. 13 (left) shows the mean stress of the first instability $\overline{\sigma}_{first}$ as a function of the tubes' gauge length for different geometries during the isothermal loading. Error bars indicate the standard deviations of the stress. Thicker tubes (i.e., Dt5, Dt10, Dt12, D2, and D3) that exhibit BUB or GB + LB1 have a relatively constant stress of the first instabilities, which indicates that in this range of lengths the L_g has insignificant influence on the occurrence of global instabilities. There is a correlation between σ_{first} and the beginning of the transformation, at which the slope of the stress–strain curve starts to decrease into the plateau. More specifically, the first global instabilities occur right after the beginning of the transformation (see Table 2). This is in accordance with the classical buckling theory, in which structures with a lower tangent modulus tend to buckle at a lower stress. For the thicker tubes (i.e., Dt5, Dt10, Dt12, D2, and D3) the values of σ_{first} vary slightly between the tubes of a different cross-section, which is closely related to the deviations between the stresses of the beginning of the transformation $\sigma_{tr,s}$ among different tubes (see Table 2) and this has a direct relation to the manufacturing process of the tubes and their microstructure. More specifically, the amount of cold work and annealing that the tube received during manufacturing process affects grain's size and orientation causing anisotropy (see Appendix B for more details on the microstructure). Nevertheless, one can see that the Dt17 tubes have a declining trend of σ_{first}, which means that the beginning of local instabilities is dependent on the L_g. It can be concluded that by increasing the gauge length of the Dt17 tube, the stress σ_{first} asymptotically approaches the approximate value of $\sigma_{tr,s}$ due to the prevalent GB + LB1 buckling mode shape that is exhibited by longer tubes. Note that for short Dt17 tubes (8 mm and below) the first instability occurs near the end or at around the middle of the transformation. For the Dt25 tubes, we were unable to determine the first occurrence of instability by the eye inspection of VE images due to small amplitudes and fast transition to failure (the data shown in Fig. 13 (left) therefore correspond to the $\sigma_{failure}$). It has to be noted

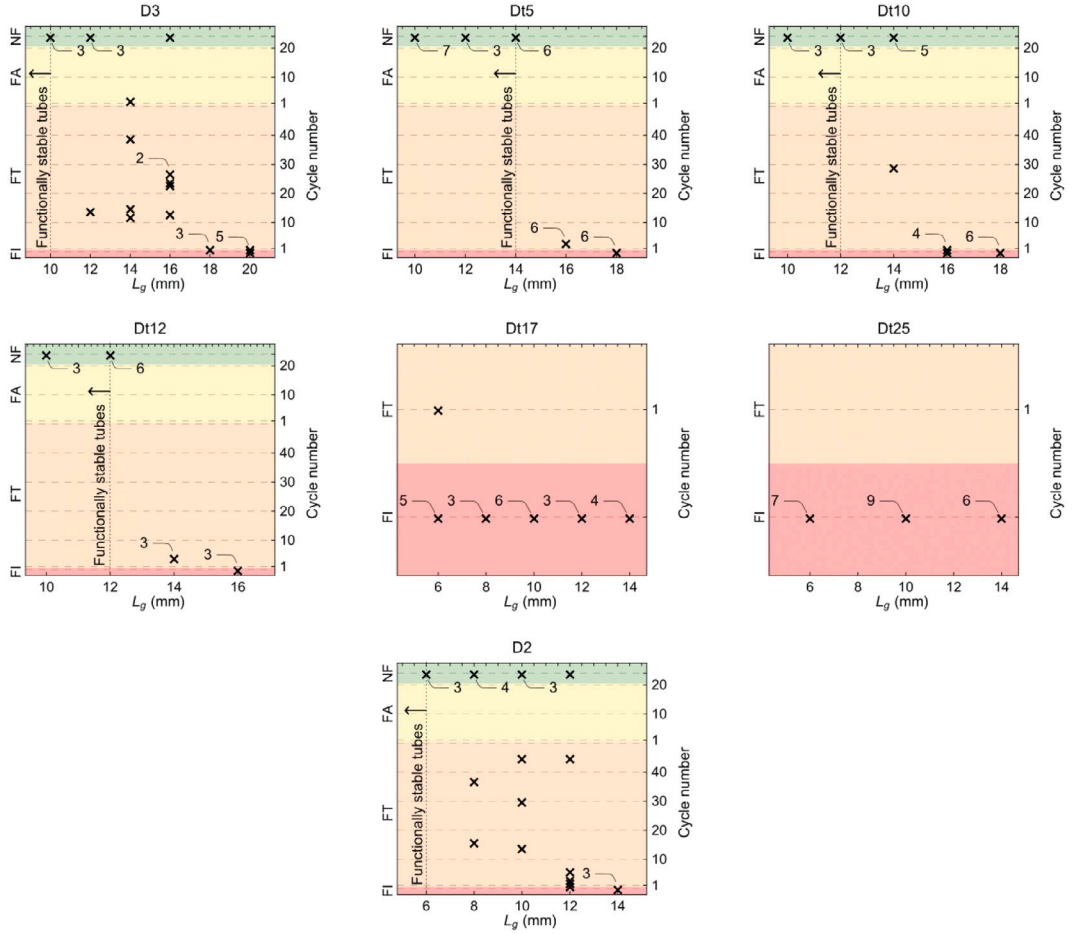

Fig. 12. Cycle number of failure as a function of gauge length L_g for tubes of different cross-sections with marked area of functionally stable tubes. Call-out number indicates the number of samples that failed at identical loading cycle number, while the labels mean: FI - failure at isothermal cycle, FT - failure at training cycles, FA - failure at adiabatic cycles, and NF - no failure.

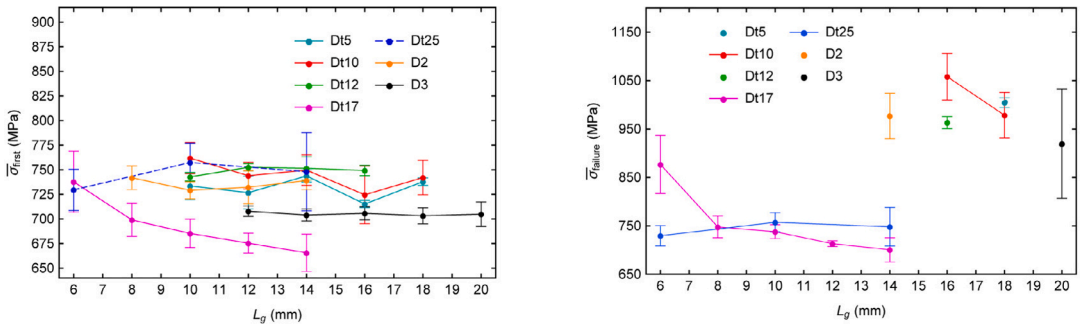

Fig. 13. Average stresses with standard deviations at the onset of the first instability during the isothermal loading as a function of the gauge length of the tube (left) and average maximum stresses with standard deviations at the failure of the tube during the isothermal loading as a function of the gauge length of the tube (right).

that the tubes with SR were not taken into account for the statistical analysis of σ_{first}.

For the tubes that failed during the isothermal loading the maximal stresses σ_{failure} were determined. In Fig. 13 (right) mean failure stresses $\overline{\sigma}_{\text{failure}}$ with standard deviations as a function of the tubes' gauge length is shown. For thick tubes (i.e. Dt5, Dt10, Dt12, D2, and D3) there are only a few points in the diagram since longer tubes than the ones that already failed were not tested (note that the goal was to define the functionally stable tubes that could potentially be used in an elastocaloric device). It should be further noted that shorter thick tubes do not fail during the isothermal loading, while for shorter thin tubes (i.e. Dt17 and Dt25) this is not the case. As indicated by the red line for the Dt10 tube and purple line for the Dt17 tube in Fig. 13 (right), the longer tube corresponds to lower stress that the tube can withstand. The smaller D_{out} means that shorter would be the tube that fails first during isothermal loading for the tubes of constant D_{out}/t, as indicated by points D2, Dt12, and D3 (although their slenderness is similar: 21.5, 19.7, and 20.5, respectively). For thick tubes of identical D_{out} (see Dt5 and Dt10 at L_g = 18 mm or Dt10 and Dt12 at L_g = 16 mm in Fig. 13 (right)), the higher the D_{out}/t ratio is, the shorter would be the tube that fails first, while the stress σ_{failure} is lower for the same lengths. The Dt17 tubes have a decreasing trend of σ_{failure} with increasing gauge length and lower absolute stress values σ_{failure} compared to thick tubes. As mentioned in the previous paragraph, the

lower absolute stress values of failure can be a consequence of different parameters of the manufacturing process resulting in different grain sizes and orientations. The Dt25 tubes have similar σ_{failure} values as the Dt17 ones, however, they do not exhibit a declining trend. This is a consequence of the fast occurrence of failure of the tubes right at the beginning of the transformation. Therefore, for the Dt25 tubes stresses σ_{failure} are similar to σ_{first}. For easier comparison, σ_{failure} for the Dt25 tube is also shown in Fig. 13 (left) with dashed blue line.

4. Conclusions

In this work we determined the dimensions of the functionally stable tubes, which could be used in durable elastocaloric devices. We performed a systematic investigation of buckling stability of tubes with an approximately constant ratio $D_{\text{out}}/t = 12$ and different D_{out} (i.e. 2 mm, 2.5 mm, and 3 mm) and tubes with constant $D_{\text{out}} = 2.5$ mm and D_{out}/t, ranging between 5 and 25. In total, 161 samples were tested with gauge lengths varying between 6 and 20 mm. Our loading procedure consisted of 3 parts due to the fact that in elastocaloric devices SMA elements are subjected to cyclic loading and instabilities may arise not only in the first loading cycles, but during subsequential cycling as well (Porenta et al., 2020b). In the first part, the tubes were subjected to 1 isothermal loading cycle, during which the strain of the tube was measured by the in-house developed video-extensometer capable of capturing a precise isothermal stress–strain response. These stress–strain responses of the tubes will be used in the subsequent studies as a reference in numerical simulations of buckling and for material parameters identification. In the second part, the tubes were subjected to 50 training cycles with the intention to stabilize/train their SE response. During cycling, we monitored whether a failure of the tube occurred and in that case what type of buckling mode shape was present. We have observed 7 different responses: stable response, buckling–unbuckling, global buckling, a combination of global and local (snap-through) buckling, local buckling with 2 circumferential waves, local buckling with 3 circumferential waves, and uncategorized local buckling. In the third part, the tubes were subjected to 20 adiabatic cycles to simulate the loading conditions that normally occur in an elastocaloric device. Interestingly, a great majority of the tubes that survived training also survived adiabatic cycles, which indicates that training alone might be a suitable measure for determining functionally stable tubes. Furthermore, some tubes that exhibited buckling–unbuckling during the first part of the loading procedure have survived the whole loading procedure. This shows that even though the tube is not completely stable, it is still functionally stable and can be used in elastocaloric devices. Finally, we constructed the phase diagrams of buckling mode shapes with characteristic areas identified for the tubes of constant $D_{\text{out}} = 2.5$ mm in λ - D_{out}/t space and for the tubes of approximately constant ratio $D_{\text{out}}/t = 12$ in λ - D_{out} space. The most important features in these phase diagrams are marked areas of functionally stable tubes that give the design guidance for future developments of the elastocaloric devices and other applications, such as dampers and actuators. More specifically, in compression-loaded elastocaloric devices it is crucial to use tubes with the longest possible length that are still functionally stable, while wall thickness of the tube should be as thin as possible in order to enlarge the heat transfer area and improve the heat transfer. Thus, functionally stable tubes with higher D_{out}/t ratio are preferred. In our recent paper (Ahčin et al., 2022) an example of the tube-based compression-loaded elastocaloric device was presented and in such configuration the selection of suitable thin-walled functionally stable tubes is crucial for high cooling or heat-pumping performance. The constructed phase diagrams show that the functionally stable tubes with $D_{\text{out}} = 2.5$ mm have maximal gauge length of 14 mm at $D_{\text{out}}/t = 5$ and 12 mm at $D_{\text{out}}/t = 12$, while tubes with $D_{\text{out}} = 3$ mm and $D_{\text{out}} = 2$ mm at $D_{\text{out}}/t = 12$ have maximal gauge lengths of 10 mm and 6 mm, respectively. On the other hand, tubes with $D_{\text{out}} = 2.5$ mm and $D_{\text{out}}/t \geq 17$ are not functionally stable due to the presence of local buckling in case of tubes shorter than 12 mm, while longer tubes prevalently exhibit global buckling. Interestingly, unstable tubes with $D_{\text{out}} = 2.5$ mm and $D_{\text{out}}/t \leq 12$ do not exhibit local buckling at first; only after severe global buckling the transition to local snap-through buckling is observed.

Based on the obtained stress–strain responses of the tubes our future work will involve material parameter identification and verification of numerical model (Porenta et al., 2021). Utilization of a verified numerical model will allow us to obtain phase diagrams, which will not be limited only to dimensions of the tubes that we could obtain for the purposes of this study, but for arbitrary tube geometries. Areas of functionally stable tubes on these phase diagrams will narrow the set of suitable tubes for elastocaloric cooling devices and will take us one step further towards identifying the optimal tube geometry.

Declaration of competing interest

The authors declare that they have no known competing financial interests or personal relationships that could have appeared to influence the work reported in this paper.

Data availability

Data will be made available on request.

Acknowledgments

This work was supported by European Research Council (ERC) under Horizon 2020 research and innovation program (ERC Starting Grant No. 803669). The authors would like to thank the anonymous reviewers for their valuable comments and suggestions.

Appendix A. Video-extensometer strain measurements and their uncertainties

During the setup, attention must be paid to the positioning of the camera. First, the axis of the tube must be vertical with respect to the camera's sensor to grant axial displacements of the tube only in vertical y-direction (see Fig. A.14). Second, the tube should be in focus over the whole gauge length of the tube. The measurement consists of two parts: experimental data acquisition, where images of the tube are captured at 1 Hz, and software data processing. Data processing begins with the definition of two regions of interest (ROIs), one at each end of the tube (see Fig. A.14), at the first captured frame. Next, the developed software detects the contours of the ROIs using gray-scale thresholds on the upsampled image and calculates the center of the contour. Then, the process is repeated for all captured frames. As a result, positions of ROIs centers (and also positions of the top and bottom edges of the contours) for each frame are obtained. This forms a baseline for all further calculations. To evaluate strains the displacements (in pixels) should be used directly:

$$\varepsilon = \frac{\Delta L}{L}, \tag{A.1}$$

where L is the initial length in pixels between center of ROIs on undeformed sample and ΔL are measured displacement in pixels:

$$\Delta L = p_{\text{ROI2}} - p_{\text{ROI1}}, \tag{A.2}$$

where p_{ROI1} and p_{ROI2} are relative positions of centers of ROI1 and ROI2 during experiments, respectively:

$$p_{\text{ROI}\alpha} = p^{i}_{\text{ROI}\alpha} - p^{1}_{\text{ROI}\alpha}, \tag{A.3}$$

where superscript i indicates frame number ($i \geq 1$) and $p^{1}_{\text{ROI}\alpha}$ is the initial position of the center. Subscript $\alpha = 1$ refers to ROI1 and $\alpha = 2$ refers to ROI2.

In order for the measured quantities to be trustworthy, their uncertainty (UC) must be evaluated. The UC of strain depends on the

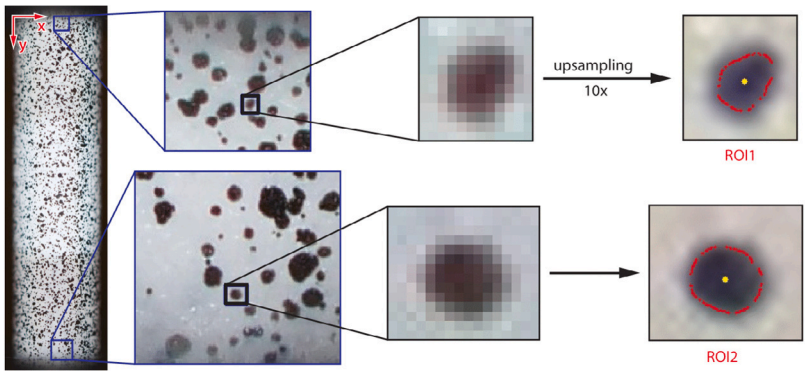

Fig. A.14. Determining the center position of ROIs: Selection of ROIs, utilizing upsampling of the image, contour detection (red), and visualization of the center (yellow).

UC of a specific measurement (experiment) due to the fact that it is a dimensionless quantity. The UC of a specific measurement is derived through the oscillation of the measured height of ROIs. It is assumed that strains of ROIs are below the VE measuring range, which means that the height of ROI should be constant. The height of the ROI $h_{\mathrm{ROI},\alpha}$ is obtained as:

$$h_{\mathrm{ROI}\alpha} = p_{\mathrm{ROI}\alpha,\mathrm{ue}} - p_{\mathrm{ROI}\alpha,\mathrm{le}}, \tag{A.4}$$

where subscripts "ue" and "le" refer to the upper and lower edge, respectively, while p is the position of the edge. UC of the height of ROI is defined as the standard deviation of the height during the experiment:

$$u_{h\mathrm{ROI}\alpha,\mathrm{exp}} = s\left[h_{\mathrm{ROI}\alpha}\right]. \tag{A.5}$$

UC of specific measurement is equal to combined UC of ROI's height, which is defined as:

$$u_{h\mathrm{ROI}\alpha,\mathrm{c}} = \sqrt{\left(u_{h\mathrm{ROI}\alpha,\mathrm{exp}}\right)^2 + \left(u_{h\mathrm{ROI}\alpha,\mathrm{dig}}\right)^2}, \tag{A.6}$$

where $u_{h\mathrm{ROI}\alpha,\mathrm{dig}}$ is the UC due to digitization and is evaluated as:

$$u_{h\mathrm{ROI}\alpha,\mathrm{dig}} = \sqrt{2}\sqrt{\left(u_{\mathrm{edge}}\right)^2 + \left(u_{\mathrm{res}}\right)^2}, \tag{A.7}$$

where u_{edge} is UC of detection of ROIs' edge position in stationary state and has a value of 0.3 pixels, while u_{res} is the UC due to image resolution and is calculated as:

$$u_{\mathrm{res}} = \frac{a_{\mathrm{res}}}{\sqrt{3}} = 0.05774\,\mathrm{px}, \tag{A.8}$$

where error a_{res} is 0.1 pixels, due to 10× upsampling of the image. Strain ε is an indirectly measured quantity, therefore its UC is calculated as:

$$u_{\varepsilon} = \sqrt{\left(u_{\Delta L}\, c_1\right)^2 + \left(u_L\, c_2\right)^2}, \tag{A.9}$$

where it is assumed that the UC of initial length (u_L) is identical to the UC of displacements ($u_{\Delta L}$), where $u_{\Delta L}$ is based on combined UC of ROIs' height (Eq. (A.6)) and is calculated as:

$$u_{\Delta L} = \sqrt{\left(u_{\mathrm{hROI1,\,c}}\right)^2 + \left(u_{\mathrm{hROI2,\,c}}\right)^2}, \tag{A.10}$$

while constants c_1 and c_2 are defined as:

$$c_1 = \frac{\partial \varepsilon}{\partial \Delta L} = L^{-1}, \tag{A.11}$$

$$c_2 = \frac{\partial \varepsilon}{\partial L} = -(\Delta L)\, L^{-2}. \tag{A.12}$$

Fig. A.15 shows the UCs of strains for all samples used in our experiments as a function of gauge length L_{g}. Interestingly, the UC of strain decreases with the length of the tube.

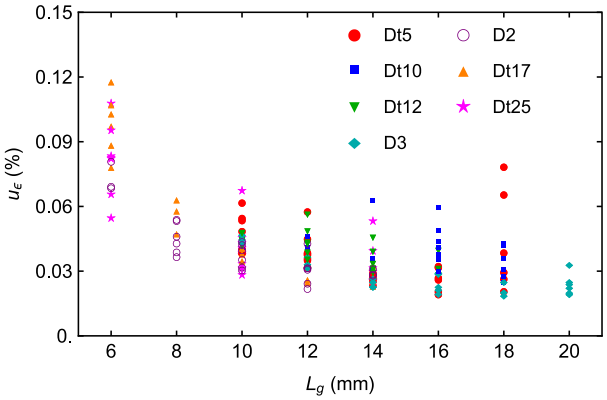

Fig. A.15. Uncertainties of measured strains for all samples as a function of gauge length L_g.

Appendix B. Microstructure of tubes

The microstructure was investigated on three tubes with different cross-sections (i.e. Dt5, Dt12, and Dt25) in order to assess the grain size and the orientation of the grains. First, a flat surface was created along the length of tubes by fine polishing. Next, an etching solution was applied to the surface of the tube with a cotton swab. After etching samples were ultrasonically cleaned in distilled water. Due to different grain sizes of the tubes each tube was exposed to a different amount of etching solution, i.e. 48 swabs for Dt5, 60 swabs for Dt12, and 72 swabs for Dt25. We used aqueous etching solution as suggested in (Undisz et al., 2011): 7.4% HF, 18.5% HNO_3 and 74.1% H_20. According to the manufacturer of the acids, the concentrations of HNO_3 and HF acids are 65% and 40%, respectively. Note that the etching solution was freshly mixed and used immediately after mixing.

The microstructure was observed with a Zeiss Axiolab 5 optical microscope equipped with an Axiocam 208 color camera and polarizer. We were able to observe the grains only by polarized light at a specific angle and magnification. Fig. B.16 shows the microstructure of the tubes. The grains are the most clearly visible on the Dt5 tube, while grains of the Dt25 tube are barely visible. The reason for that is the different amount of cold work received by the material during the manufacturing process. Thinner tubes are exposed to more stages of deforming and annealing (the exact manufacturing process is unknown), therefore the grains are smaller and more elongated. This affects the energy of the grain boundary in a way that etching solution corrodes the grain boundary as well as the grain, therefore the border of the grain is less visible. Due to the same reason we were not able to obtain visible grains on the surface of the tube perpendicular to its axis.

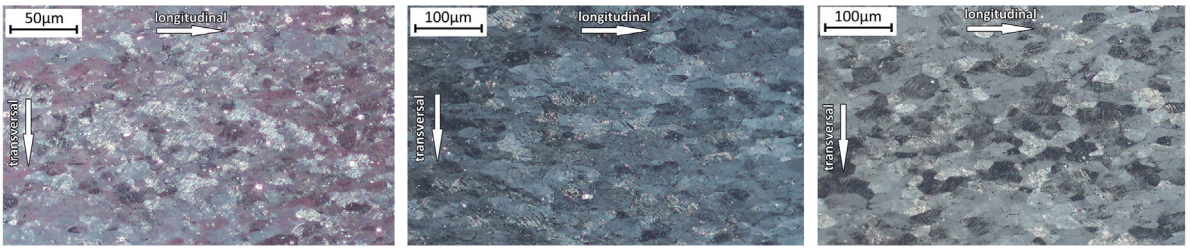

Fig. B.16. Grains of the tubes: Dt25 at 200× magnification (left), Dt12 at 100× magnification (middle) and Dt5 at 100× magnification (right).

Table B.3
Number of intercepts per unit length of test line in longitudinal and transversal direction with their averages, ASTM grain size numbers and average grain diameters.

Tube	N_{Ll} (mm^{-1})	N_{Lt} (mm^{-1})	$\overline{N}_L$ (mm^{-1})	G	$\overline{d}$ (μm)
Dt5	52.2	80.2	68.1	8.9	15.9
Dt12	56.1	85.8	69.4	8.9	15.9
Dt25	134.0	221.8	172.4	11.6	6.7

Determination of average grain size was done according to ASTM standard E112-13 (ASTM Standard, 2013) using the intercept method. For non-equiaxed grain shapes in round bars and tubes, the intercept method is applied on radial, longitudinal and transverse sections. In our case radial section is omitted due to the inability to obtain visible grains. Therefore, Table B.3 shows only the numbers of intercepts per unit length of test line in longitudinal (N_{Ll}) and traversal (N_{Lt}) directions. Average number of intercept $\overline{N}_L$ and ASTM grain size number G are obtained using Eqs. (B.1) and (B.2), respectively. Average grain diameter is taken from ASTM standard, Tab. 4 (ASTM Standard, 2013). Interestingly, Dt5 and Dt12 tubes have similar grain sizes, while Dt12 tube has more elongated grains. On the other hand, Dt25 tube have smaller grains that are severely elongated indicating a large amount of cold work during the production process.

$$\overline{N}_L = \left(N_{Ll} \cdot N_{Lt}\right)^{1/2} \tag{B.1}$$

$$G = \left(6.643856 \log_{10} \bar{N}_L\right) - 3.288 \tag{B.2}$$

Appendix C. Preliminary tests

Preliminary tests were conducted in order to determine three important aspects/features of the experimental procedure. First, the determination of isothermal strain rates; second, the minimal number of training cycles for temperature stable and repeatable adiabatic cycles; and third, necessary holding time in adiabatic cycles for stabilization of the temperature of the sample with the surrounding temperature. All mentioned aspects were determined by measuring temperature changes of the sample during the loading–unloading procedure. Temperature changes were measured in the middle of the tube by FLIR A6750sc infrared camera with an absolute accuracy of ±2% of the reading, equipped with a lens of 50 mm focal length and a 640 × 512 pixel IR sensor with a spatial resolution of 15 μm.

We used samples with gauge length of 12 mm, outer diameter of 3 mm, and inner diameter of 2.5 mm, that were coated with a thin layer of LabIR paint for standard application with emissivity of 0.92. For determination of isothermal conditions tubes were loaded from 0 to 1150 MPa with strain rates of 0.0001, 0.0002, and 0.0003 s^{-1} that correspond to loading speeds of 0.0012, 0.0024, and 0.0036 mm/s. During the loading, the tubes were exposed to forced convection with air in order to increase heat transfer between the tube and the surroundings. Corresponding temperature changes are shown in Fig. C.17. For the purpose of this work, we decided isothermal conditions are met when temperature differences do not exceed ±1 °C, and therefore strain rate of 0.0003 s^{-1} was selected for isothermal tests.

The isothermal procedure was followed by training cycles, where two tubes were loaded from 0 to 1150 MPa with strain rates of 0.008 s^{-1}. The first one was subjected to 30 training cycles and the second one to 50 training cycles. After that, a few adiabatic cycles followed, where both tubes were loaded from 0.05 mm to maximal relative displacement at the last training cycle at a strain rate of 0.07 s^{-1}. After each loading and unloading 10 s holding time (at constant displacement) was enforced in order for the temperature of the tube to stabilize with the surroundings. The temperature changes of the tubes during adiabatic cycling are shown in Fig. C.18. The temperature changes of the tube exposed to 30 training cycles are decreasing with each adiabatic cycle (see Fig. C.18 (a)) from 32 °C in the first loading to 24 °C at the last (fourth) loading cycle. On the other hand, in case of the tube exposed to 50 training cycles, temperature changes are almost constant during loading and unloading at approximately +25 °C and −20 °C, respectively (see Fig. C.18 (b)). With that, 50 training cycles are accepted to be the margin for training (stabilization) of the tube's response. Detailed view of loading and unloading temperature changes (Fig. C.18 (c) and (d)) verifies, that 10 s holding time is enough for the temperature of the tube to be stabilized with the surroundings (note that the sample was exposed to the forced heat convection with air). It also confirms that strain rate of 0.07 s^{-1} results in adiabatic response due to sufficient increase of temperature (see the Supplementary material of (Porenta et al., 2020b), where experiments with systematic changes of strain rate were performed to identify adiabatic strain rate limit of the identical tube as used our case).

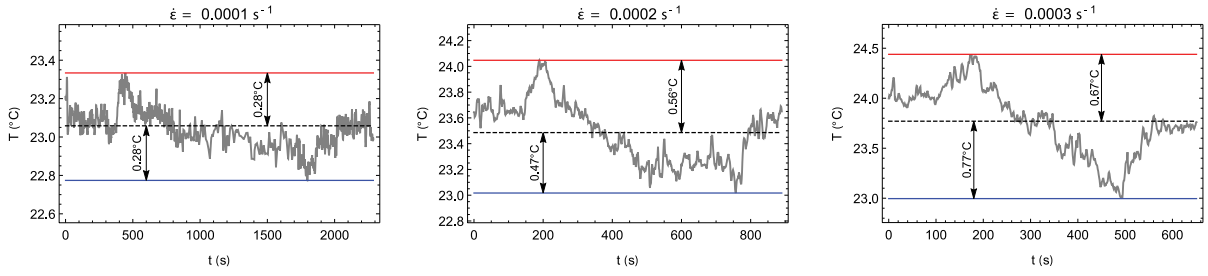

Fig. C.17. Temperature changes during preliminary tests at strain rates: 0.0001 s^{-1} (left), 0.0002 s^{-1} (middle) and 0.0003 s^{-1} (right).

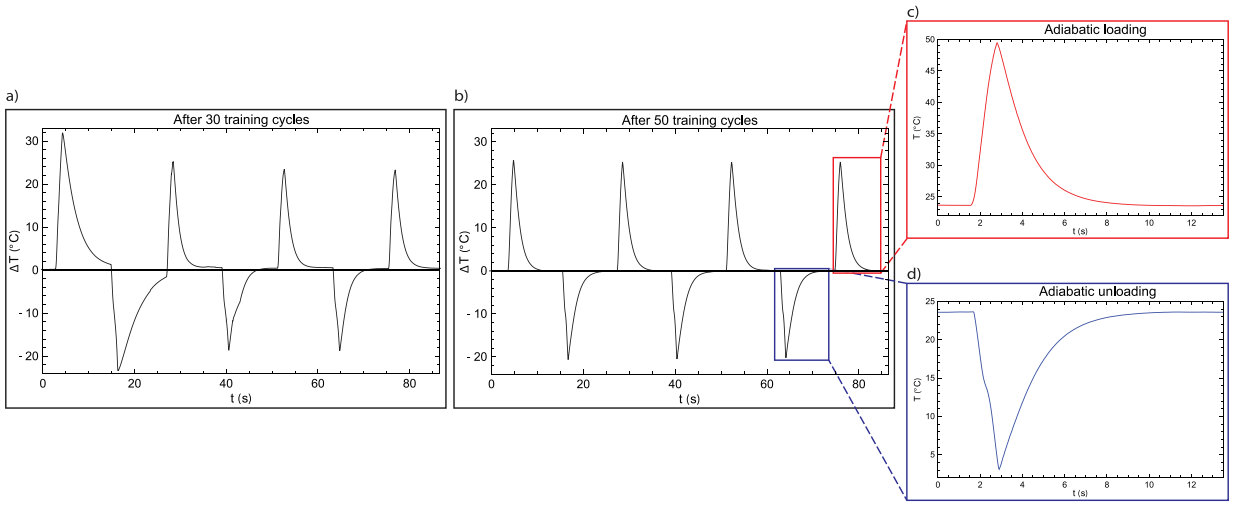

Fig. C.18. Adiabatic temperature changes during preliminary tests: (a) after 30 training cycles, (b) after 50 training cycles, (c) stable adiabatic temperature response during loading and (d) stable adiabatic temperature response during unloading.

Appendix D. Uncategorized local buckling modes

Different local buckling modes were observed during the experiments. Among them we categorized LU2 and LU3, while the rest belong to a group of uncategorized local buckling modes labeled as LU. On Fig. D.19, a few uncategorized local buckling modes are shown for Dt25 tubes with gauge lengths of 10 and 14 mm.

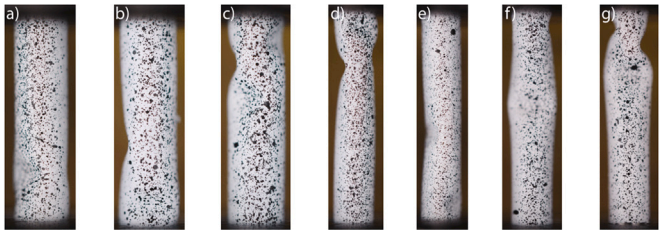

Fig. D.19. Uncategorized local buckling modes of Dt25 tubes: (a - c) $L_g = 10$ mm and (d - g) $L_g = 14$ mm.

Appendix E. Supplementary data

Supplementary material related to this article can be found online at https://doi.org/10.1016/j.ijsolstr.2022.111948.

References

Ahčin, Ž., Dall'olio, S., Žerovnik, A., Žvar Baškovič, U., Porenta, L., Kabirifar, P., Cerar, J., Zupan, S., Brojan, M., Klemenc, J., Tušek, J., 2022. High Performance and Fatigue-Resistant Elastocaloric Regenerator for Efficient Cooling and Heat-Pumping, Available At SSRN 4135686.

Ahčin, Ž., Liang, J., Engelbrecht, K., Tušek, J., 2021. Thermo-hydraulic evaluation of oscillating-flow shell-and-tube-like regenerators for (elasto) caloric cooling. Appl. Therm. Eng. 190, 116842.

Asfaw, A.M., Sherif, M.M., Xing, G., Ozbulut, O.E., 2020. Experimental investigation on buckling and post-buckling behavior of superelastic shape memory alloy bars. J. Mater. Eng. Perform. 29 (5), 3127–3140.

ASTM Standard, 2013. E112-13 standard test methods for determining average grain size. In: Active Standard ASTM E112. ASTM International West Conshohocken, PA.

Bachmann, N., Fitger, A., Maier, L.M., Mahlke, A., Schäfer-Welsen, O., Koch, T., Bartholomé, K., 2021. Long-term stable compressive elastocaloric cooling system with latent heat transfer. Commun. Phys. 4 (1), 1–6.

Chen, J., Lei, L., Fang, G., 2021. Elastocaloric cooling of shape memory alloys: A review. Mater. Today Commun. 28, 102706.

Chen, J., Zhang, K., Kan, Q., Yin, H., Sun, Q., 2019. Ultra-high fatigue life of NiTi cylinders for compression-based elastocaloric cooling. Appl. Phys. Lett. 115 (9), 093902.

Coativy, G., Haissoune, H., Seveyrat, L., Sebald, G., Chazeau, L., Chenal, J.-M., Lebrun, L., 2020. Elastocaloric properties of thermoplastic polyurethane. Appl. Phys. Lett. 117 (19), 193903.

Cong, D., Xiong, W., Planes, A., Ren, Y., Mañosa, L., Cao, P., Nie, Z., Sun, X., Yang, Z., Hong, X., et al., 2019. Colossal elastocaloric effect in ferroelastic Ni-Mn-Ti alloys. Phys. Rev. Lett. 122 (25), 255703.

Coral, W., Rossi, C., Colorado, J., Lemus, D., Barrientos, A., 2012. SMA-based muscle-like actuation in biologically inspired robots: A state of the art review. Smart Actuation Sens. Syst.-Recent Adv. Future Chall. 53–82.

Damanpack, A., Bodaghi, M., Liao, W., 2018. Snap buckling of NiTi tubes. Int. J. Solids Struct. 146, 29–42.

Engelbrecht, K., Tušek, J., Sanna, S., Eriksen, D., Mishin, O.V., Bahl, C.R., Pryds, N., 2016. Effects of surface finish and mechanical training on Ni-Ti sheets for elastocaloric cooling. APL Mater. 4 (6), 064110.

Greibich, F., Schwödiauer, R., Mao, G., Wirthl, D., Drack, M., Baumgartner, R., Kogler, A., Stadlbauer, J., Bauer, S., Arnold, N., et al., 2021. Elastocaloric heat pump with specific cooling power of 20.9 W g^{-1} exploiting snap-through instability and strain-induced crystallization. Nat. Energy 6 (3), 260–267.

Hou, H., Cui, J., Qian, S., Catalini, D., Hwang, Y., Radermacher, R., Takeuchi, I., 2018. Overcoming fatigue through compression for advanced elastocaloric cooling. MRS Bull. 43 (4), 285–290.

Ianniciello, L., Bartholomé, K., Fitger, A., Engelbrecht, K., 2022. Long life elastocaloric regenerator operating under compression. Appl. Therm. Eng. 202, 117838.

Jani, J.M., Leary, M., Subic, A., Gibson, M.A., 2014. A review of shape memory alloy research, applications and opportunities. Mater. Des. (1980-2015) 56, 1078–1113.

Jiang, D., Bechle, N.J., Landis, C.M., Kyriakides, S., 2016a. Buckling and recovery of NiTi tubes under axial compression. Int. J. Solids Struct. 80, 52–63.

Jiang, D., Landis, C.M., Kyriakides, S., 2016b. Effects of tension/compression asymmetry on the buckling and recovery of NiTi tubes under axial compression. Int. J. Solids Struct. 100, 41–53.

Kabirifar, P., Žerovnik, A., Ahčin, Ž., Porenta, L., Brojan, M., Tušek, J., 2019. Elastocaloric cooling: State-of-the-art and future challenges in designing regenerative elastocaloric devices. Stroj. Vestn./J. Mech. Eng. 65.

Kim, Y., Jo, M.-G., Park, J.-W., Park, H.-K., Han, H.N., 2018. Elastocaloric effect in polycrystalline $Ni_{50}ti_{45.3}v_{47}$ shape memory alloy. Scr. Mater. 144, 48–51.

Kirsch, S.-M., Welsch, F., Michaelis, N., Schmidt, M., Wieczorek, A., Frenzel, J., Eggeler, G., Schütze, A., Seelecke, S., 2018. NiTi-based elastocaloric cooling on the macroscale: From basic concepts to realization. Energy Technol. 6 (8), 1567–1587.

Lagoudas, D.C., 2008. Shape Memory Alloys: Modeling and Engineering Applications. Springer Science & Business Media.

Mañosa, L., Planes, A., 2017. Materials with giant mechanocaloric effects: Cooling by strength. Adv. Mater. 29 (11), 1603607.

Miyazaki, S., Imai, T., Igo, Y., Otsuka, K., 1986. Effect of cyclic deformation on the pseudoelasticity characteristics of Ti-Ni alloys. Metall. Trans. A 17 (1), 115–120.

Moya, X., Kar-Narayan, S., Mathur, N.D., 2014. Caloric materials near ferroic phase transitions. Nature Mater. 13 (5), 439–450.

Navigant Consulting Inc., 2014. Energy savings potential and RD&D opportunities for non-vapor-compression HVAC technologies. http://dx.doi.org/10.2172/1220817, URL https://www.osti.gov/biblio/1220817.

Nemat-Nasser, S., Choi, J.Y., Isaacs, J.B., Lischer, D.W., 2006. Quasi-static and dynamic buckling of thin cylindrical shape-memory shells. J. Appl. Mech. 73 (5), 825–833.

Ozbulut, O., Hurlebaus, S., Desroches, R., 2011. Seismic response control using shape memory alloys: A review. J. Intell. Mater. Syst. Struct. 22 (14), 1531–1549.

Pereiro-Barceló, J., Bonet, J.L., 2017. Ni-Ti SMA bars behaviour under compression. Constr. Build. Mater. 155, 348–362.
Petrini, L., Migliavacca, F., 2011. Biomedical applications of shape memory alloys. J. Metall. 2011.
Porenta, L., Brank, B., Dujc, J., Brojan, M., Tušek, J., 2020a. A shell finite element model for superelasticity of shape memory alloys. In: Analysis of Shells, Plates, and Beams. Springer, pp. 373–388.
Porenta, L., Kabirifar, P., Žerovnik, A., Čebron, M., Žužek, B., Dolenec, M., Brojan, M., Tušek, J., 2020b. Thin-walled Ni-Ti tubes under compression: ideal candidates for efficient and fatigue-resistant elastocaloric cooling. Appl. Mater. Today 20, 100712.
Porenta, L., Lavrenčič, M., Dujc, J., Brojan, M., Tušek, J., Brank, B., 2021. Modeling large deformations of thin-walled SMA structures by shell finite elements. Commun. Nonlinear Sci. Numer. Simul. 101, 105897.
Qian, S., Geng, Y., Wang, Y., Ling, J., Hwang, Y., Radermacher, R., Takeuchi, I., Cui, J., 2016a. A review of elastocaloric cooling: Materials, cycles and system integrations. Int. J. Refrig. 64, 1–19.
Qian, S., Geng, Y., Wang, Y., Muehlbauer, J., Ling, J., Hwang, Y., Radermacher, R., Takeuchi, I., 2016b. Design of a hydraulically driven compressive elastocaloric cooling system. Sci. Technol. Built Environ. 22 (5), 500–506.
Rahman, M.A., Qiu, J., Tani, J., 2001. Buckling and postbuckling characteristics of the superelastic SMA columns. Int. J. Solids Struct. 38 (50–51), 9253–9265.
Rahman, M.A., Qiu, J., Tani, J., 2005. Buckling and postbuckling characteristics of the superelastic SMA columns – numerical simulation. J. Intell. Mater. Syst. Struct. 16 (9), 691–702.
Richter, F., Kastner, O., Eggeler, G., 2011. Finite-element simulation of the anti-buckling-effect of a shape memory alloy bar. J. Mater. Eng. Perform. 20 (4), 719–730.
Schmidt, M., Schütze, A., Seelecke, S., 2015. Scientific test setup for investigation of shape memory alloy based elastocaloric cooling processes. Int. J. Refrig. 54, 88–97.
Shen, Y., Wei, Z., Sun, W., Zhang, Y., Liu, E., Liu, J., 2020. Large elastocaloric effect in directionally solidified all-d-metal Heusler metamagnetic shape memory alloys. Acta Mater. 188, 677–685.
Šittner, P., Heller, L., Pilch, J., Curfs, C., Alonso, T., Favier, D., 2014. Young's modulus of austenite and martensite phases in superelastic NiTi wires. J. Mater. Eng. Perform. 23 (7), 2303–2314.
Snodgrass, R., Erickson, D., 2019. A multistage elastocaloric refrigerator and heat pump with 28 K temperature span. Sci. Rep. 9 (1), 1–10.
Suzuki, S., Urushiyama, Y., Taya, M., 2004. Energy absorption material using buckling strength of shape memory alloy plate. In: Smart Structures and Materials 2004: Active Materials: Behavior and Mechanics, Vol. 5387. International Society for Optics and Photonics, pp. 218–227.
Tang, Z., Li, D., 2012a. Experimental investigation of axial impact buckling response of pseudo-elastic NiTi cylindrical shells. Int. J. Impact Eng. 39 (1), 28–41.
Tang, Z., Li, D., 2012b. Quasi-static axial buckling behavior of NiTi thin-walled cylindrical shells. Thin-Walled Struct. 51, 130–138.
Tušek, J., Engelbrecht, K., Eriksen, D., Dall'Olio, S., Tušek, J., Pryds, N., 2016. A regenerative elastocaloric heat pump. Nat. Energy 1 (10), 1–6.
Tušek, J., Engelbrecht, K., Mikkelsen, L.P., Pryds, N., 2015. Elastocaloric effect of Ni–Ti wire for application in a cooling device. J. Appl. Phys. 117 (12), 124901.
Tušek, J., Žerovnik, A., Čebron, M., Brojan, M., Žužek, B., Engelbrecht, K., Cadelli, A., 2018. Elastocaloric effect vs fatigue life: Exploring the durability limits of Ni-Ti plates under pre-strain conditions for elastocaloric cooling. Acta Mater. 150, 295–307.
Ulpiani, G., Bruederlin, F., Weidemann, R., Ranzi, G., Santamouris, M., Kohl, M., 2020. Upscaling of SMA film-based elastocaloric cooling. Appl. Therm. Eng. 180, 115867.
Undisz, A., Reuther, K., Reuther, H., Rettenmayr, M., 2011. Occurrence and origin of non-martensitic acicular artifacts on NiTi. Acta Mater. 59 (1), 216–224.
Urushiyama, Y., Lewinnek, D., Qiu, J., Tani, J., 2001. Buckling of curved column and twinning deformation effect. In: IUTAM Symposium on Smart Structures and Structronic Systems. Springer, pp. 283–290.
Urushiyama, Y., Lewinnek, D., Qiu, J., Tani, J., 2003. Buckling of shape memory alloy columns. JSME Int. J. Ser. A Solid Mech. Mater. Eng. 46 (1), 60–67.
Watkins, R., 2015. Thermomechanical Characterization and Modeling of Superelastic Shape Memory Alloy Beams and Frames (Ph.D. thesis). University of Michigan.
Watkins, R.T., Reedlunn, B., Daly, S., Shaw, J.A., 2018. Uniaxial, pure bending, and column buckling experiments on superelastic NiTi rods and tubes. Int. J. Solids Struct. 146, 1–28.
Watkins, R.T., Shaw, J.A., 2018. Unbuckling of superelastic shape memory alloy columns. J. Intell. Mater. Syst. Struct. 29 (7), 1360–1378.
Xiao, F., Bucsek, A., Jin, X., Porta, M., Planes, A., 2022. Giant elastic response and ultra-stable elastocaloric effect in tweed textured Fe–Pd single crystals. Acta Mater. 223, 117486.
Xiao, Y., Jiang, D., 2022. Buckling and unbuckling of superelastic NiTi tube. Acta Mech. Solida Sin. 1–14.
Xie, Z., Sebald, G., Guyomar, D., 2017. Temperature dependence of the elastocaloric effect in natural rubber. Phys. Lett. A 381 (25–26), 2112–2116.
Xu, S., Huang, H.-Y., Xie, J., Takekawa, S., Xu, X., Omori, T., Kainuma, R., 2016. Giant elastocaloric effect covering wide temperature range in columnar-grained $Cu_{71.5}$ $Al_{17.5}Mn_{11}$ shape memory alloy. APL Mater. 4 (10), 106106.
Zhang, K., Kang, G., Sun, Q., 2019. High fatigue life and cooling efficiency of NiTi shape memory alloy under cyclic compression. Scr. Mater. 159, 62–67.
Zhang, S., Yang, Q., Li, C., Fu, Y., Zhang, H., Ye, Z., Zhou, X., Li, Q., Wang, T., Wang, S., et al., 2022. Solid-state cooling by elastocaloric polymer with uniform chain-lengths. Nature Commun. 13 (1), 1–7.